



## Photocatalytic O<sub>2</sub> activation enhancement and algae inactivation mechanism of BiO<sub>2-x</sub>/Bi<sub>3</sub>NbO<sub>7</sub> van der Waals heterojunction

Dongyu Xu <sup>a,1</sup>, Geng Li <sup>b,1</sup>, Yilin Dong <sup>a</sup>, Qiuwen Wang <sup>a</sup>, Jie Zhang <sup>a</sup>, Tongsa Yang <sup>a</sup>, Shaoxuan Pang <sup>a</sup>, Guangming Zhang <sup>a</sup>, Longyi Lv <sup>a</sup>, Yuguo Xia <sup>c</sup>, Zhijun Ren <sup>a,\*</sup>, Pengfei Wang <sup>a,\*</sup>

<sup>a</sup> Tianjin Key Laboratory of Clean Energy and Pollutant Control, School of Energy and Environmental Engineering, Hebei University of Technology, Tianjin 300401, China

<sup>b</sup> National Supercomputer Center in Tianjin, Tianjin 300457, China

<sup>c</sup> School of Chemistry and Chemical Engineering, National Engineering Research Center for Colloidal Materials, Shandong University, Jinan 250100, China



### ARTICLE INFO

#### Keywords:

Photocatalytic oxygen activation  
BiO<sub>2-x</sub>/Bi<sub>3</sub>NbO<sub>7</sub>  
Van der Waals heterojunction  
Algae inactivation  
Reactive oxygen species

### ABSTRACT

The removal of algae by reactive oxygen species (ROS) through photocatalytic O<sub>2</sub> activation is still a challenge. Herein, we constructed a van der Waals (VDW) heterojunction photocatalyst by coupling BiO<sub>2-x</sub> with Bi<sub>3</sub>NbO<sub>7</sub> for photocatalytic inactivation of *Microcystic aeruginosa* and photodegradation of Microcystin-LR. The oxygen vacancies in BiO<sub>2-x</sub>/Bi<sub>3</sub>NbO<sub>7</sub> can effectively promote the chemisorption of O<sub>2</sub>, and the VDW force can drive the photoelectrons in Bi<sub>3</sub>NbO<sub>7</sub> transfer to BiO<sub>2-x</sub> through S-scheme transfer path, resulting more electrons reduce O<sub>2</sub> to O<sub>2</sub><sup>-</sup>. Hence, photocatalytic inactivation of algae by BiO<sub>2-x</sub>/Bi<sub>3</sub>NbO<sub>7</sub> is 14.17 and 19.05 times higher than BiO<sub>2-x</sub> and Bi<sub>3</sub>NbO<sub>7</sub>, respectively. During the photocatalysis, the O<sub>2</sub><sup>-</sup> damages the antioxidant system and cell membrane of algae, resulting in the release of organic matter and Microcystin-LR and finally causing the death of algae. The three-dimensional fluorescence spectroscopy indicates BiO<sub>2-x</sub>/Bi<sub>3</sub>NbO<sub>7</sub> can further available photodegrade the organic matter, and four possible photodegradation pathways of MC-LR are proposed.

### 1. Introduction

Recently, harmful algal blooms widely occur in the whole world caused by eutrophication of water bodies, which pose serious threat to social, ecological and human security [1]. The rapid and massive reproduction of algae results in the serious damages the aquatic plant and the ecosystem. Even more serious is the algal toxins produced after the death of algae which can directly lead to the death of water animal or plant. Furthermore, the algal toxins also can harm the human health by the biological enrichment in food chain or drinking water [2]. *Microcystic aeruginosa* (*M. aeruginosa*) which is a representative freshwater algae species has aroused much concern. And its metabolite Microcystin-LR (MC-LR) is the most toxic and common microcystins [3]. Hence, it is urgency and important to develop effective methods for inactivation of *M. aeruginosa* and degradation of MC-LR from water.

Photocatalytic technology has been widely used to effectively remove algae, which has the ability of activating molecular oxygen (O<sub>2</sub>) to generate reactive oxygen species (ROS), such as superoxide (·O<sub>2</sub><sup>-</sup>), hydroxyl (·OH), singlet oxygen (<sup>1</sup>O<sub>2</sub>), and hydrogen peroxide (H<sub>2</sub>O<sub>2</sub>)

[4], and ROS plays crucial roles in inactivation of algae. Nevertheless, the ROS evolution efficiency is still far from satisfactory, primarily on account of the poor specific adsorption of O<sub>2</sub> and fewer effective electrons resulted by inefficiency electron transfer from photocatalyst to O<sub>2</sub> [5]. Defect engineering is recognized to be an important factor that enhances photocatalytic O<sub>2</sub> activation [6]. Among these defects, oxygen vacancy in metal oxides has caused widespread concern, since it can provide the coordinatively unsaturated sites with low-valence metal species for the chemical adsorption of O<sub>2</sub>. This strategy can construct a valid channel for the transfer of the electrons to adsorbed O<sub>2</sub>, and also weakens the O=O, which effectively promote O<sub>2</sub> activation [7]. Besides, compared to their bulk counterpart, ultrathin 2D materials are easier to expose oxygen vacancies and reduce the photogenerated electrons migration distance thus enhancing the capacity of electrons transfer [8]. Although oxygen vacancies have many benefits, some studies also reported their limitations. In generally, oxygen vacancies may act as charge recombination centers [9]. In this case, though the channel still exists, the number of electrons from photocatalyst to O<sub>2</sub> will decrease thus giving rise to poorer activity. Hence, to attain high photocatalytic

\* Corresponding authors.

E-mail addresses: [renzhijun2003@126.com](mailto:renzhijun2003@126.com) (Z. Ren), [pengfeiwang@hebut.edu.cn](mailto:pengfeiwang@hebut.edu.cn) (P. Wang).

<sup>1</sup> D.Y. Xu and G. Li contributed equally to this work.

$O_2$  activation in defected photocatalysts, effective strategies are needed to enhance the electron shortage.

To increase the number of electrons from photocatalyst to  $O_2$ , a valid strategy is to construct heterojunctions, which enables visibly suppress the recombination of photogenerated charge-carriers [10–12]. Li et al. constructed the heterojunctions photocatalysts by coupling oxygen-vacancy-rich  $CeO_{2-x}$  with  $AgI$ , and immensely enhanced the photocatalytic activity for degrading tetracycline, which was 3 and 47 times higher than  $CeO_2$  and  $AgI$ , respectively [13]. However, the heterojunction constructed by bulk materials has poor interface contact, which reduces the number of electrons transfer between the photocatalysts. Therefore, constructing heterojunction by coupling a 2D oxygen vacancy-based photocatalysts to a 2D ultrathin nanosheets may be an efficient strategy to solve the problem of the poorer contact area, namely 2D/2D van der Waals (VDW) heterojunction. It exhibits enormous merits in the photocatalytic applications: i) the unique face-face contact with immense interfacial area and strong interactions; ii) the optimized electronic structure owing to the intimate electronic coupling; iii) the increased interfacial charge separation and migration between layers [14,15]. However, up to now, few studies of the effects of oxygen vacancy-based VDW heterojunctions have been done to completely investigate on photocatalytic  $O_2$  activation.

Herein, by taking 2D/2D VDW heterojunction of  $BiO_{2-x}/Bi_3NbO_7$  ( $O_v$ -BO/BNO) as a typical model system, we confirm that constructing 2D/2D VDW heterojunction with oxygen vacancy can significantly facilitate the photocatalytic  $O_2$  activation, and the novel photocatalyst displays the excellent photocatalytic inactivation of algal cells and degradation of MC-LR. Advanced characterizations, such as in-situ irradiation X-ray photoelectron spectroscopy (IS-XPS), combined with density function theory (DFT) calculations reveal the strong electronic coupling interactions are presented between BNO and  $O_v$ -BO by VDW forces. Furthermore, under visible light the removal capacity of algae by the  $O_v$ -BO/BNO is investigated. The effects of  $O_v$ -BO/BNO on algal cell morphologies and membrane permeability, cell organic matters, phycoobiliproteins, antioxidant system, lipid peroxidation and metabolic activities are analyzed for making out the possible algae inhibition mechanism. Meanwhile, the probable photodegradation pathways of MC-LR are presented and the aquatic toxicity of MC-LR and transformation intermediates are assessed.

## 2. Experimental section

### 2.1. Preparation of photocatalysts and characterization

#### 2.1.1. Preparation of photocatalysts

$BiO_{2-x}$ ,  $Bi_3NbO_7$  nanosheet and  $BiO_{2-x}/Bi_3NbO_7$  heterojunction composites were prepared by a simple solvothermal method. Details for synthesizing photocatalysts are shown in Section S1.

#### 2.1.2. Characterization

The X-ray diffraction (XRD) patterns were analyzed by a Rigaku D/Max 2200PC X-ray diffractometer ( $Cu K\alpha$ ,  $\lambda = 0.15418$  nm) to obtain the crystalline structure of the photocatalysts. Thermo Nicolet iS5 fourier transform infrared spectra (FTIR) spectrometer equipped with a liquid-nitrogen-cooled MCT detector was employed to measure the FTIR spectra of the photocatalysts. The electron paramagnetic resonance (EPR) spectrometer (A300–10/12, Bruker) was employed to record the oxygen vacancy of samples. The electron spin resonance (ESR) spectrometer (JES-FA200, Bruker) was conducted to detect the reactive oxygen species. The transmission electron microscopy (TEM, a JEOL JEM-2100 F) was used to examine the morphology and microstructure of the prepared samples at an accelerating voltage of 200 kV. Atomic force microscopy (AFM) images were obtained by using a Bruker Multi-Mode 8 AFM with peak force tapping-mode with peak force tapping-mode. The component elements and chemical states of the samples were determined by X-ray photoelectron spectroscopy (XPS, ESCALAB 250Xi). The

binding energies were calibrated using C 1 s peak at 284.6 eV. And in situ irradiated X-ray photoelectron spectroscopy (ISI-XPS) was carried out on an electron spectrometer (ESCALAB 210, VG, UK) to research the electron density changes on photocatalysts under light irradiation. UV-vis spectrophotometer (U-3900 H, HITACHI Corporation of Japan) was used measuring UV-Vis absorption spectra. Photoluminescence (PL) spectra were measured on a Fluorescence spectrometer (FL3-22). And the FLS920 fluorescence lifetime spectrophotometer recorded the time-resolved PL (TRPL) decay curves. The IPCE1000 surface photovoltage spectroscopy was used to obtain the surface photovoltage (SPV) spectrum. The systems contain a lockin amplifier and a simple chamber. All the processes were conducted under normal atmospheric pressure and at room temperature, and monochromatic source was offered by 500 W xenon lamp (CHF-XQ-500 W). The intermediates generated of MC-LR were recorded using liquid chromatography-mass spectrometry (LC-MS).

### 2.2. Theoretical calculation and photoelectrochemical measurements

Density function theory (DFT) calculations corrected by onsite Coulomb interaction were conducted by using the Vienna ab initio simulation package (VASP) [16,17]. Generalized gradient approximation (GGA) with the Perdew-Burke-Ernzerhof (PBE) functional calculate the exchange-correlation interaction, and the wave functions were expanded in a plane wave basis [18]. The energy cutoff was set to as of 500 eV. For all the calculations, the convergence criteria for the electronic is 10–5 eV and the ionic relaxation is 0.02 eV/Å. For the construction of surface models, A vacuum of 20 Å was carrying out excluding interactions between periodic images. To analyze the VDW interaction, the DFT-D2 method of Grimme was employed and the work function is defined as  $\Phi = E_V - E_F$  (in which  $E_V$  and  $E_F$  are the electrostatic potentials of the vacuum and Fermi levels, respectively). Furthermore, the details of photoelectrochemical measurements are displayed in Section S2.

### 2.3. *M. aeruginosa* inactivation experiment

The cultivation of *M. aeruginosa* cells is displayed in Section S3. The photocatalytic reactor of *M. aeruginosa* inactivation can be seen in Fig. S1 and the photocatalytic inactivation efficiency of *M. aeruginosa* was determined by the changes of chlorophyll a content (Section S4). In the process of photocatalytic reaction, a 300 W xenon lamp (CEL-HXF300, Beijing Zhongjiaojinyuan, China) equipped with 420 nm cutoff filter was used as the light source. 30 mg photocatalyst was dispersed in 150 mL of algae suspension. Then, before visible-light irradiation the suspension stirred in the dark for 30 min to exclude the effects of adsorption. The whole photocatalytic inactivation experiment was carried out for 150 min under constantly magnetic stirring, and at 30 min interval 5 mL algae solution was sampled for further treatment. Furthermore, the MC-LR photocatalytic degradation experiments were also carried out, and the experiments on the studies of multiple factors, recycle photocatalytic experiment and quenching experiment was also applied (Section S5). And the acute and chronic toxicities of the degradation intermediates were evaluated by using calculated data from the ECOSAR program (Section S6). During the photocatalysis, the inactivation of *M. aeruginosa* was assessed from the aspects of algal cellular morphologies and membrane permeability, cellular organics, total soluble protein, photosynthetic system, antioxidant systems of algae (Section S7-S12).

## 3. Results and discussion

### 3.1. Photocatalysts synthesis and characterization

The fabrication procedure of the composite photocatalyst is schematically depicted in Fig. 1a. The  $BiO_{2-x}/Bi_3NbO_7$  ( $O_v$ -BO/BNO)

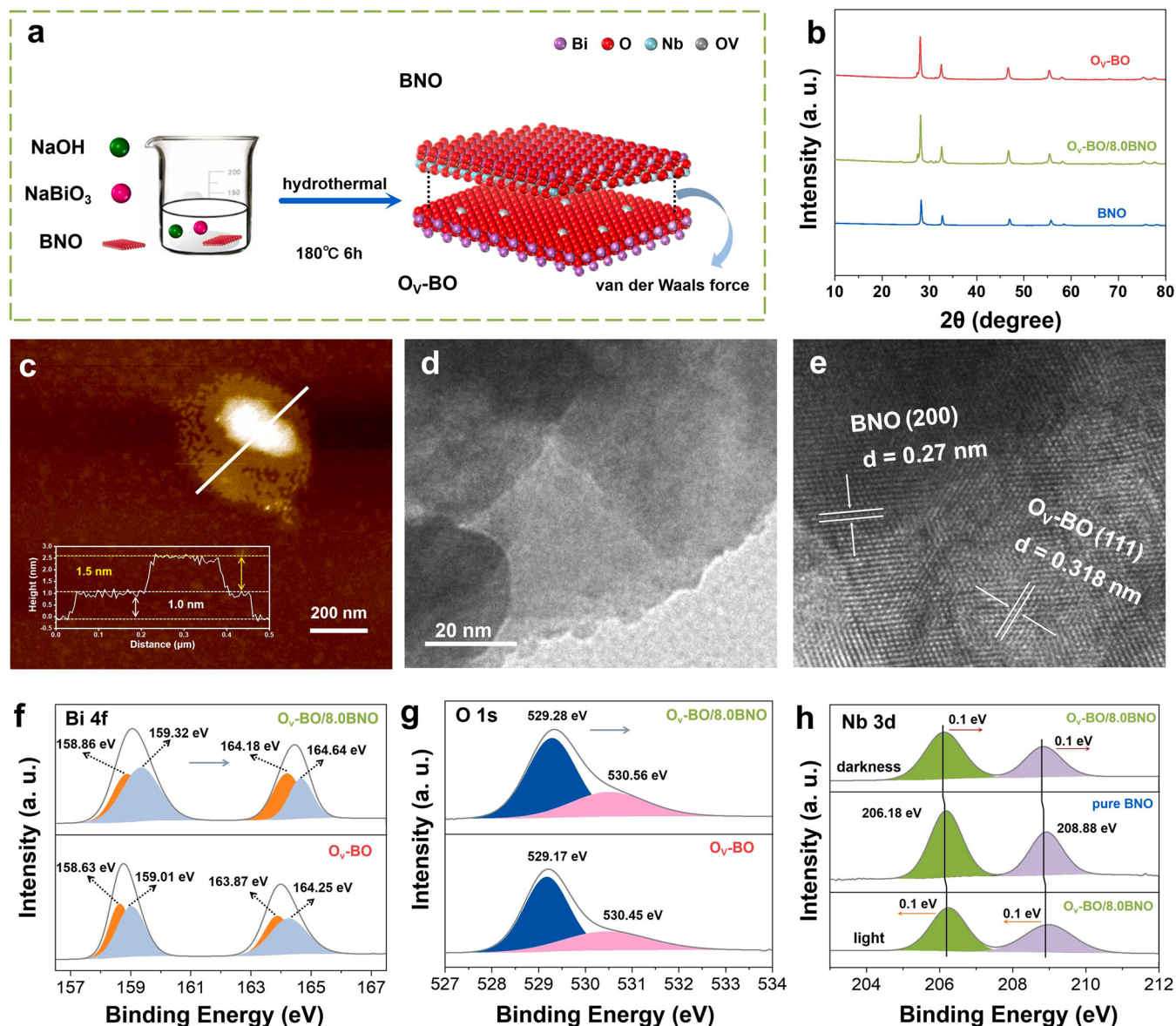


**Fig. 1.** (a) Schematic illustration of the formation process for Ov-BO/BNO composite photocatalysts. (b) XRD spectra of Ov-BO, Ov-BO/8.0BNO and BNO. (c) AFM image of Ov-BO/8.0BNO. (d) TEM and (e) HRTEM images of Ov-BO/8.0BNO. High-resolution XPS spectra of the prepared samples: (f) Bi 4f and (g) O 1s and (h) High-resolution Nb 3d XPS spectra of BNO and Ov-BO/8.0BNO samples tested in darkness and under illumination ( $\lambda = 365$  nm).

composite nanosheets were hydrothermally synthesized with Bi<sub>3</sub>NbO<sub>7</sub> and NaBiO<sub>3</sub> at 180 °C for 6 h. Fig. 1b and S2 show that the X-ray diffraction (XRD) spectra indicate the modification of Ov-BO by BNO exerts no obvious influence on the peaks of Ov-BO, because the relatively weak interaction between Ov-BO and BNO cannot change the crystal structure of Ov-BO [19]. Furthermore, Ov-BO/8.0BNO also shows similar fourier transform infrared spectra (FTIR) spectra, proving the unchanged molecular structure of Ov-BO after combined with BNO (Fig. S3). Meanwhile, in order to confirm the presence of OVs in Ov-BO and Ov-BO/8.0BNO, electron paramagnetic resonance (EPR) spectra were carried out (Fig. S4). The intensity of EPR signal did not decrease in Ov-BO/8.0BNO compared with Ov-BO, indicating that constructing heterojunction did not reduce the number of oxygen vacancies.

Atomic force microscopy (AFM) analysis confirms the ultrathin nanosheet structures of Ov-BO and BNO with a thickness of 1.5 nm and 1.0 nm, respectively (Fig. S5a and S5b). As displayed in Fig. 1c and S5c-d, the bottom layer with a thickness of ca. 1.0 nm can be attributed to BNO nanosheets and the upper layer with a thickness of ca. 1.5 nm can

be indexed to the Ov-BO nanosheets. These results prove that Ov-BO stacks on BNO to form Ov-BO/8.0BNO heterojunction, which offers the support of the formation of VDW heterojunction between the two 2D materials. Moreover, the transmission electron microscopy (TEM) image of Ov-BO/8.0BNO further exhibits that partly stacked 2D ultrathin nanosheets are generated and BNO is attached on the surface of Ov-BO (Fig. 1d-e). The energy dispersive X-ray (EDX) (Fig. S6a), high-angle annular dark-field scanning TEM (HAADF-STEM) (Fig. S6b) and element mapping (Fig. 6c-f) images exhibit that Bi, O and Nb elements are well distributed within Ov-BO/8.0BNO. Overall, these results verify the co-existence of 2D Ov-BO and 2D BNO, making the fabrication of VDW heterojunction possible between the two 2D material.

The formation of 2D/2D VDW heterojunction is further confirmed by conducting the X-ray photoelectron spectroscopy (XPS) spectra, and the interactions between the Ov-BO and BNO is also uncovered. The XPS survey spectrum (Fig. S7) shows that Ov-BO/8.0BNO is composed of Bi, O and Nb elements. Fig. 1f displays that the peaks at 164.25 eV and 159.01 eV are assigned to Bi<sup>5+</sup> species and the peaks at 163.87 and

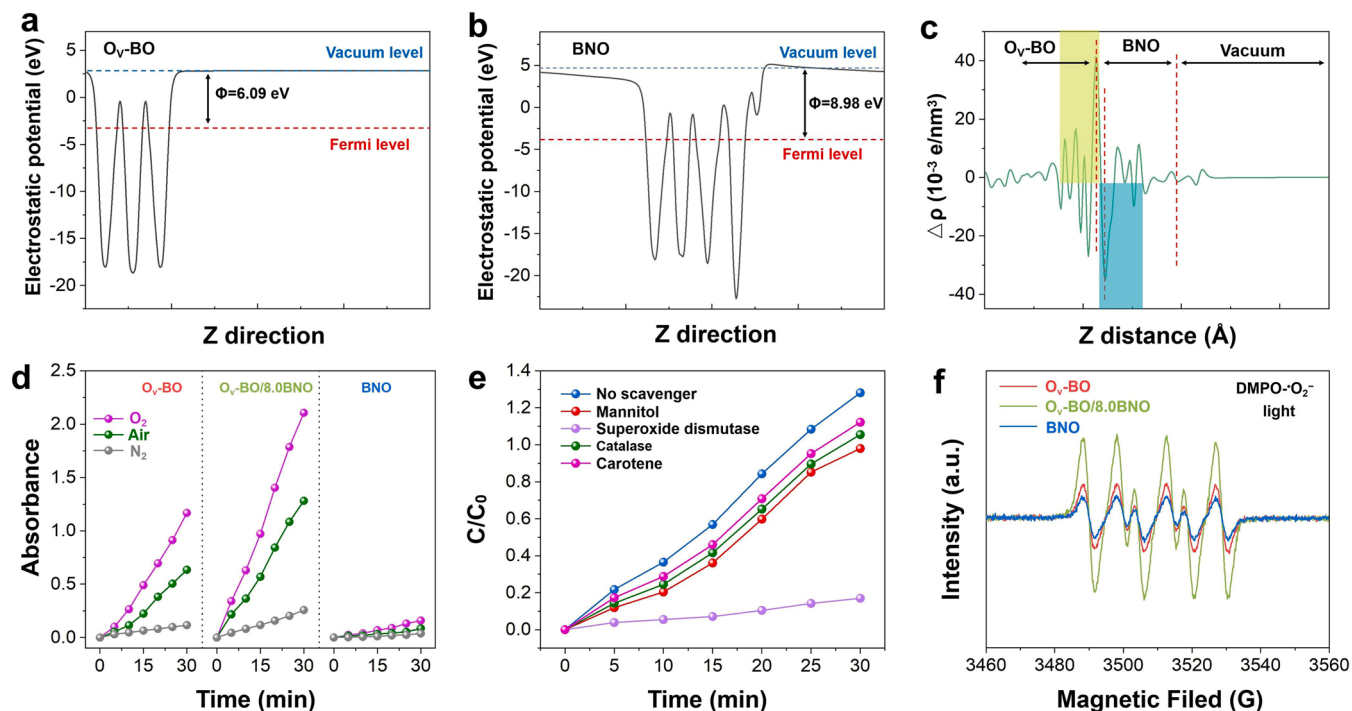


**Fig. 2.** Average potential profile along Z-axis direction for: (a) Ov-BO and (b) BNO. (c) The planar averaged charge density difference  $\Delta\rho$  along the Z-direction for the Ov-BO/BNO VDW heterojunction. The ultramarine and yellow regions represent net electron accumulation and depletion, respectively. (d) The product absorbance peak monitored at 370 nm versus reaction time under different gas conditions for Ov-BO, BNO and Ov-BO/8.0BNO. (e) Absorbance change over Ov-BO/8.0BNO with different scavengers of TMB oxidation. (f) ESR spectra of DMPO-O<sub>2</sub><sup>-</sup> under visible light obtained from Ov-BO, BNO and Ov-BO/8.0BNO systems.

158.63 eV can be ascribed to Bi<sup>3+</sup> [20]. The peaks of O 1 s located at 529.17 and 530.45 eV can be assigned to the lattice oxygen and absorbed oxygen, respectively (Fig. 1j) [21]. The oxygen vacancies on O<sub>v</sub>-BO/8.0BNO can be confirmed by the peak of absorbed oxygen, working as the activation centers to trap the photogenerated electrons and absorb O<sub>2</sub> to produce O<sub>2</sub><sup>·</sup> [22]. Fig. S7b shows the Nb 3d<sub>3/2</sub> and Nb 3d<sub>5/2</sub> peaks are situated at the binding energy positions of 206.17 and 208.92 eV, respectively, which are pertained to the Nb<sup>5+</sup> in BNO and O<sub>v</sub>-BO/8.0BNO composite [23]. These results further demonstrate that the O<sub>v</sub>-BO/BNO VDW heterojunction composite is successfully prepared. Besides, it is noticed that the Bi 4 f, O 1 s and Nb 3d peaks of O<sub>v</sub>-BO/8.0BNO all show a slight shift, indicating the strong interactions are presented between BNO and O<sub>v</sub>-BO by VDW forces [24].

### 3.2. Charge transfer of VDW heterostructure and photocatalytic oxygen activation performance

In situ irradiated X-ray photoelectron spectroscopy (ISI-XPS) spectra and density function theory (DFT) calculations were carried out to further explore the process of electron migration at the interface of O<sub>v</sub>-BO and BNO. After forming a close contact between O<sub>v</sub>-BO and BNO without illumination, the binding energies of Nb atoms in the O<sub>v</sub>-BO/8.0BNO decrease compared with BNO (Fig. 1h). This reveals that BNO works as the electron acceptor without illumination. On the contrary, under illumination the binding energies of Nb atoms in the O<sub>v</sub>-BO/8.0BNO composite increase compared with the BNO, indicating that it acts as the electron donor in the existence of illumination. These shifts of binding energy offer the direct proof of the charge carrier migration route across the O<sub>v</sub>-BO/BNO interface. To be specific, the migration of electrons from BNO to O<sub>v</sub>-BO provides evidence for the direct S-scheme mechanism. Besides, the results of DFT calculations are displayed in Fig. 2a-b. The work functions ( $\Phi$ ) of O<sub>v</sub>-BO and BNO are calculated to be 6.09 and 8.98 eV, respectively, confirming the higher Fermi level (EF) position of O<sub>v</sub>-BO compared to that of BNO. Therefore, when they contacted with each other, electrons will flow from O<sub>v</sub>-BO to BNO to

enable the phases at the same Fermi level. And interfacial built-in electric fields will be formed, making for the separation of charge carriers during the photocatalysis in O<sub>v</sub>-BO/BNO [25]. Furthermore, the three-dimensional charge density difference and planar-averaged electron density difference can further confirm this result. Fig. 2c and S8 show that near the interface O<sub>v</sub>-BO part is positively charged, whereas BNO part is negatively charged. Therefore, theoretical calculated results further powerfully corroborate that the combination of the BNO with O<sub>v</sub>-BO can effectively construct the VDW heterojunction and there is strong electron coupling effect in the O<sub>v</sub>-BO/BNO VDW heterojunction.

Furthermore, to study the photocatalytic O<sub>2</sub> activation performance of the photocatalysts, 3,3',5,5'-tetramethylbenzidine (TMB) was used to act as an indicator molecule to conduct O<sub>2</sub> activation experiments. Compared to O<sub>v</sub>-BO and BNO, O<sub>v</sub>-BO/8.0BNO shows the best O<sub>2</sub> activation ability (Fig. 2d). Meanwhile, under O<sub>2</sub>, air and N<sub>2</sub>, the apparent disparate TMB oxidation rates confirm that ROS are converted from O<sub>2</sub>. To confirm the type of ROS species, mannite, superoxide, dismutase catalase (SOD) and carotene were used as scavengers, which can suppress the generation of ·OH, O<sub>2</sub><sup>·</sup>, H<sub>2</sub>O<sub>2</sub> and <sup>1</sup>O<sub>2</sub>, respectively. Mannite, superoxide and carotene almost cannot inhibit the TMB oxidation and dismutase catalase (SOD) shows a significant restrain on TMB oxidation rates, confirming that the main ROS is O<sub>2</sub><sup>·</sup> (Fig. 2e). Meanwhile, electron spin resonance (ESR) was employed to further confirm that the main active species is O<sub>2</sub><sup>·</sup> (Fig. 2f and S9). And the enhanced signals of O<sub>2</sub><sup>·</sup> detected in O<sub>v</sub>-BO/8.0BNO indicate that the construction of VDW heterojunctions may contribute to increase the number of electrons to generate more O<sub>2</sub><sup>·</sup>, and thus enhance photocatalytic O<sub>2</sub> activation.

### 3.3. Mechanism of enhanced photocatalytic oxygen activation

To obtain insight into the photocatalytic O<sub>2</sub> activation mechanism, the optical absorption, charge separation and transfer of O<sub>v</sub>-BO/8.0BNO VDW heterojunction are considered. Firstly, the optical absorption ability of O<sub>v</sub>-BO/8.0BNO composite was studied by employing UV-vis diffuse reflectance spectroscopy. Fig. S10a shows the absorption edge of

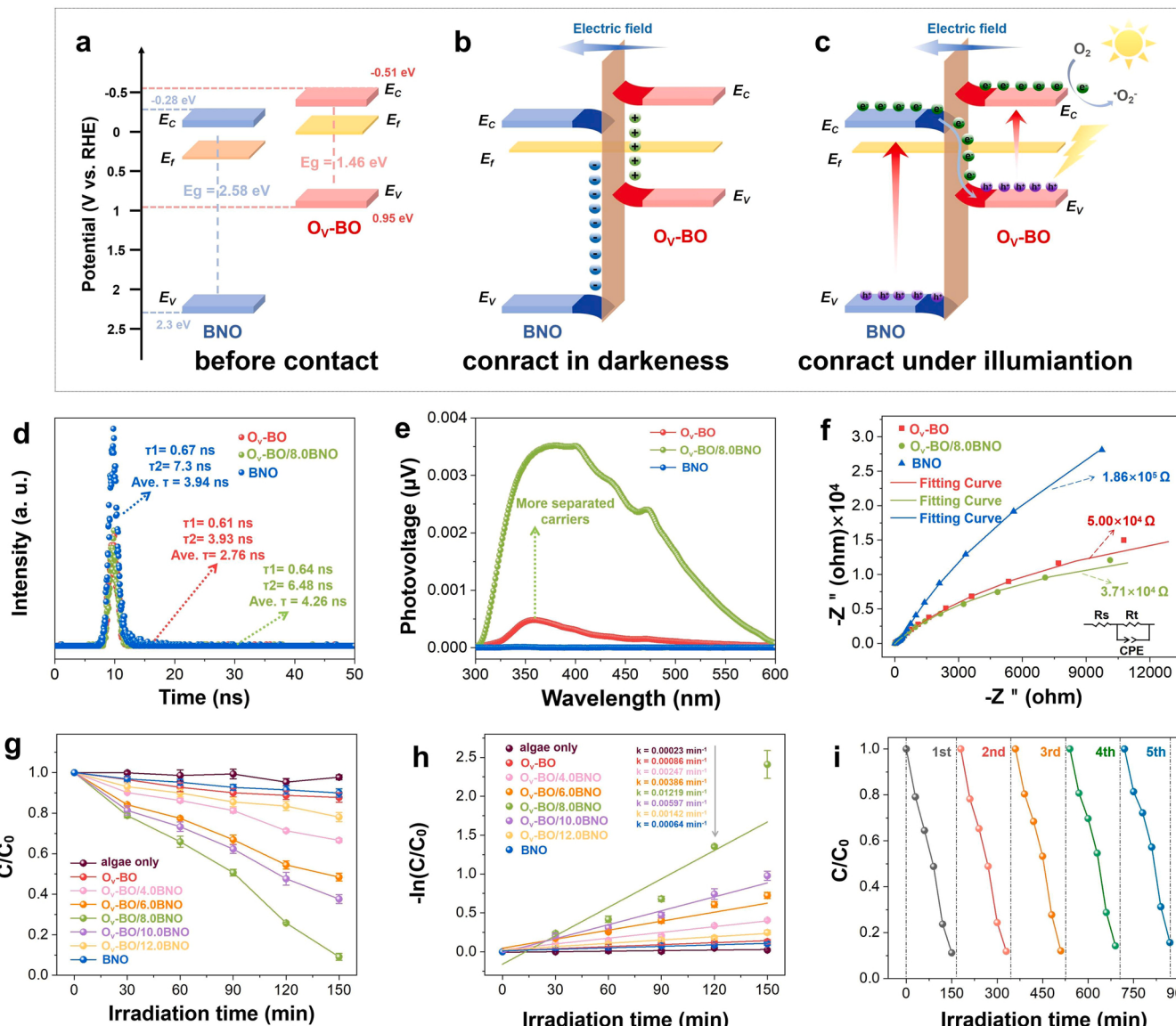


**Fig. 3.** (a) Band structures of pure BNO and Ov-BO. (b) The internal electric field with band-edge bending near the interface of BNO and Ov-BO. (c) The S-scheme transfer mechanism of photogenerated electrons under the illumination. (d) TRPL decay spectra, (e) SPV spectra and (f) EIS Nyquist plots of the BNO, Ov-BO and Ov-BO/8.0BNO, respectively. (g) The removal efficiency of chlorophyll a of the prepared samples and (h) the corresponding kinetic curves. (i) The cycle runs of Ov-BO/8.0BNO for chlorophyll a degradation under visible light irradiation. Error bars represent standard deviations from triplicate experiments ( $n = 3$ ).

Ov-BO/8.0BNO composite appears red-shift, meaning better optical absorption capability. It may due to the tightly interacted by VDW forces [24]. Furthermore, the  $E_g$  (band gap) of Ov-BO and BNO, calculated by a plot of  $(\text{hv})^2$  versus  $(\text{hv})$ , are 1.46 and 2.58 eV, respectively (Fig. S10b). Then, the valence band (VB) positions of the samples are confirmed by XPS-valence spectra. Fig. S10c shows the VB positions of Ov-BO and BNO are measured to be 0.95 and 2.3 eV, respectively. The conduction band (CB) values of Ov-BO and BNO are obtained to be  $-0.51$  and  $-0.28$  eV, respectively, by combining with the calculated bandgap value.

Hence, Fig. 3a-c demonstrate under the illumination of pure BNO and Ov-BO the schematic illustration of transfer mechanism of photogenerated electrons. When Ov-BO photocatalyst is closely touched with BNO in darkness, in order to reach the same Fermi energy level, the electrons of Ov-BO naturally flow to BNO (Fig. 3a). This is due to that Ov-BO has a higher Fermi level compared with BNO. When the electrons of Ov-BO/8.0BNO migrate through the interface, the interface region near the Ov-BO part will be positively charged due to the loss of

electrons, which will make the electrons depletion layer form and the band edge of Ov-BO bend upward. Oppositely, as displayed in Fig. 3b, owing to the acquisition of electrons, the interface region near the BNO is negatively charged, which results in forming the accumulation layer of electrons and the downward bend of band edge of BNO. Hence, the built-in electric fields established at interface of Ov-BO/8.0BNO heterojunction can impede the flow of electrons from BNO to Ov-BO. After the electrons of Ov-BO and BNO are excited under visible light, the photoelectrons accumulated in CB of BNO will recombine with the photo-generated holes in VB of Ov-BO (Fig. 3c). The advantage of this S-scheme transfer path is that it did not only separate the photogenerated electron-hole pairs in space, but also remove the relatively unnecessary photoelectrons in CB of BNO and VB in of Ov-BO. As a result, the photoelectrons will be accumulated in the CB of Ov-BO and then more electrons will transfer to  $\text{O}_2$  to generate more  $\cdot\text{O}_2^-$ .

To study the separation rate of the photogenerated electron-hole pairs and lifetime of the charge carrier, steady-state photoluminescence (PL) and time-resolved photoluminescence (TRPL) were

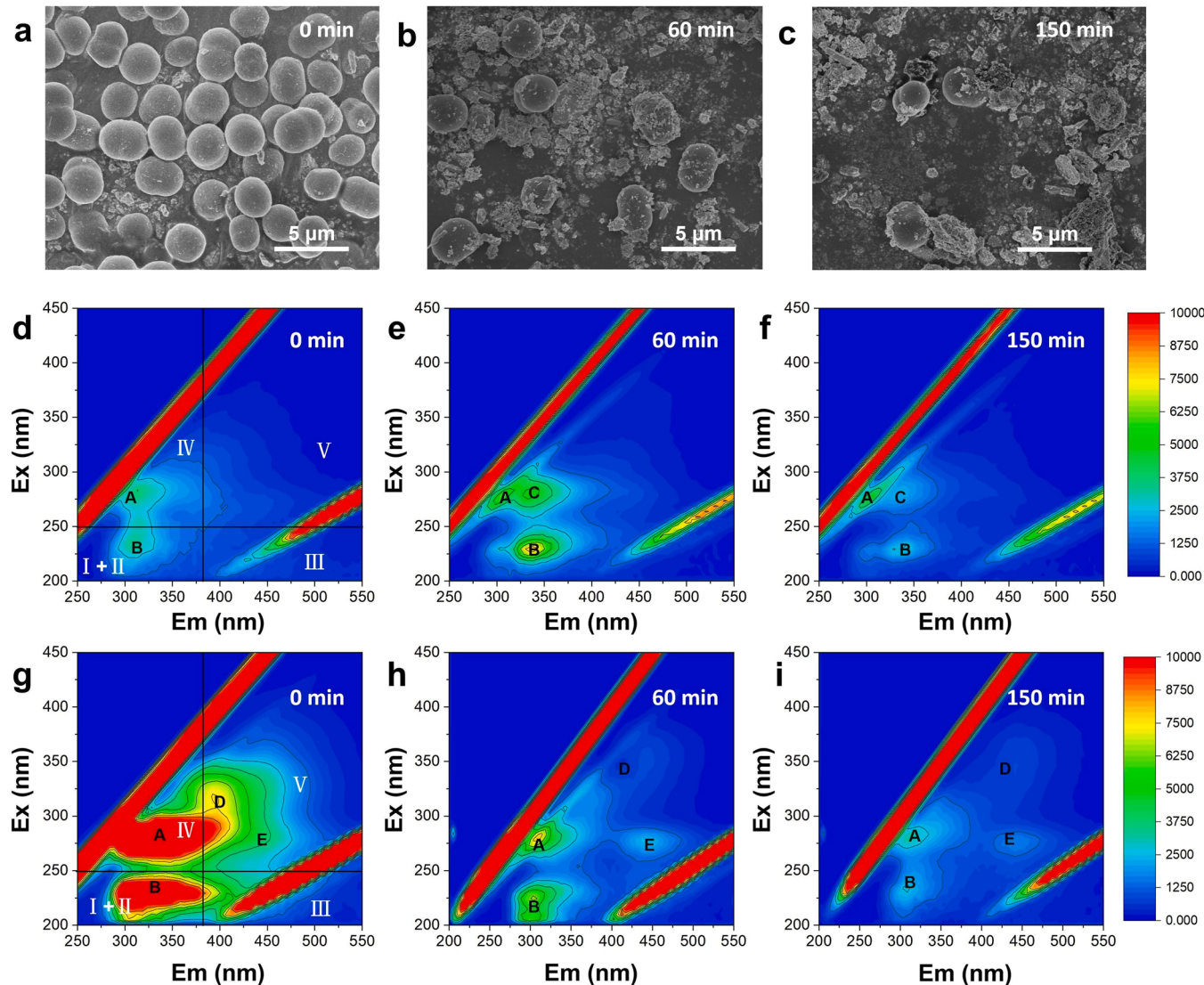


**Fig. 4.** Cellular morphologies and membrane permeability assessment of *M. aeruginosa* during the photocatalysis: (a-c) morphologies of *M. aeruginosa* during the photocatalysis. Three-dimensional fluorescence spectra of (d-f) EOM and (g-i) IOM of algal cells during the photocatalytic process at 0 min, 60 min and 150 min.

employed. Compared to Ov-BO and BNO, the quenched PL of Ov-BO/BNO is due to that the recombination of charge carrier is suppressed (Fig. S11a). This may due to that the valid charge separation and migration is realized between Ov-BO and BNO [19]. Moreover, as displayed in Fig. 3d and Table S1, Ov-BO/BNO shows the longest lifetime (4.26 ns) compared to Ov-BO and BNO, which can further suggest the higher separation and transfer ability of charge. Therefore, more electrons are able to participate in the photocatalytic O<sub>2</sub> activation, thus boosting ability of photocatalytic O<sub>2</sub> activation. Furthermore, surface photovoltage spectroscopy (SPV) further indicates the higher photovoltage on the surface of Ov-BO/BNO than that on Ov-BO and BNO, indicating the existence of BNO can enhance dissociation of photoinduced charge [26] (Fig. 3e). Subsequently, photocurrent responses and electrochemical impedance spectra (EIS) tests were carried out to attain the deep comprehend of the charge transfer behavior [27]. Fig. S11b shows the photocurrent density of Ov-BO/BNO is the highest (1.48 μA cm<sup>-2</sup>) and it is 2.03 and 5.1 times excess than Ov-BO (0.73 μA cm<sup>-2</sup>) and BNO (0.29 μA cm<sup>-2</sup>), respectively. It further confirms that excellent separation efficiency of charge in Ov-BO/BNO. Furthermore, the EIS spectra and charge-transfer resistance value are displayed in Fig. 3f and Table S2. The semicircle radius of the Nyquist plot of Ov-BO/BNO is smaller than those of Ov-BO and BNO and Ov-BO/BNO also show the

lower charge-transfer resistance value ( $R_t = 3.71 \times 10^4 \Omega$ ). These results further indicate the construction of VDW heterojunction lessen the interfacial charge transfer resistance, speeding up the charge carrier migration rate. In addition, the charge carrier density of Ov-BO/8.0BNO is 1.15 times higher than Ov-BO (Fig. S11d), which offers more evidences for promoting the electron transfer. Based on the above researches, we propose the VDW heterojunction markedly increases the charge separation and transfer ability, and offers more electrons to activate O<sub>2</sub>. Then more O<sub>2</sub> can be generated to further participate in photocatalytic reactions.

#### 3.4. Photocatalytic removal of *M. aeruginosa*

Profiting from enhanced O<sub>2</sub> activation ability for O<sub>2</sub> generation, Ov-BO/BNO is regarded as an efficient photocatalyst for the inactivation of algae. *Microcystis aeruginosa* (*M. aeruginosa*) is chosen as a model alga. As displayed in Fig. 3 g, the algae can grow normally without photocatalyst under visible light irradiation. And in Fig. 3 g the pure Ov-BO and the BNO have no influence on the algal growth. In comparison, all the Ov-BO/BNO composites display excellent ability in the process of algal inactivation. And the Ov-BO/8.0BNO exhibits the best inactivation efficiency, which can degrade the chlorophyll a by nearly 91% within

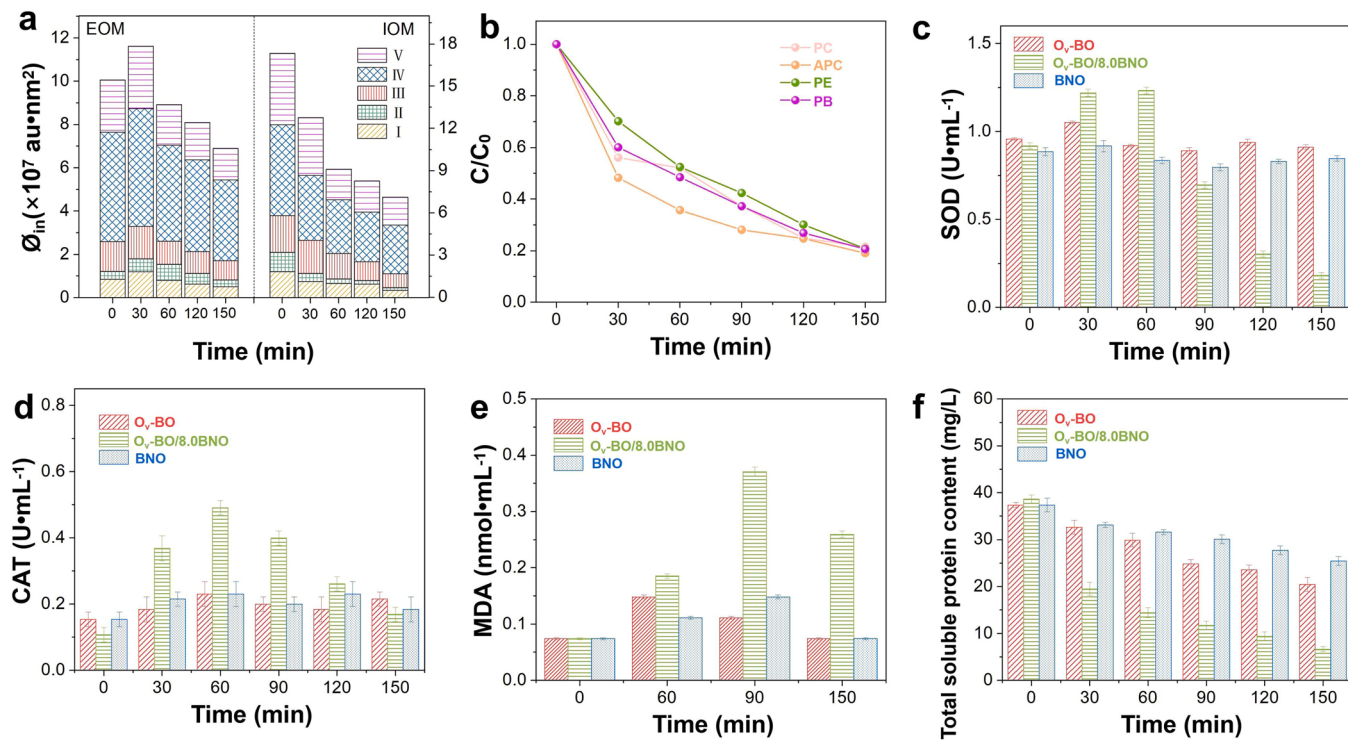


**Fig. 5.** The fluorescence regional integral of EOM and IOM during photocatalytic inactivation of *M. aeruginosa* by Ov-BO/8.0BNO. (b) Variations of the contents of phycobiliproteins during photocatalytic process by Ov-BO/8.0BNO. Effects of Ov-BO, Ov-BO/8.0BNO and BNO on the activity of *M. aeruginosa*: (c) SOD, (d) CAT, (e) MDA and (f) the total soluble protein. Error bars represent standard deviations from triplicate experiments ( $n = 3$ ).

150 min. Additionally, Fig. 3 h and Table S3 exhibit that the reaction rate constant of Ov-BO/8.0BNO ( $0.01219 \text{ min}^{-1}$ ) is 14.17 and 19.05 times higher than Ov-BO ( $0.00086 \text{ min}^{-1}$ ) and BNO ( $0.00064 \text{ min}^{-1}$ ), respectively. It is due to the better photocatalytic  $\text{O}_2$  activation of Ov-BO/8.0BNO. Furthermore, the regrowth test of the inactivated algal culture is carried out. No significant change in removal efficiency can be observed in Fig. S12a, indicating algae cells are not to be regenerate. It shows that Ov-BO/8.0BNO has the excellent ability of photocatalytic inactivation of algae. Furthermore, the optimal dosage of Ov-BO/8.0BNO is determined to be 0.03 g (Fig. S12b-c and Table S3). Meanwhile, the comparisons with other photocatalytic systems are represented in Table S4, and the Ov-BO/8.0BNO heterojunction composite still displays excellent ability of controlling the harmful algal blooms, which the time to achieve the same removal effect can be reduced to 150 min. The influence factors for photocatalytic inactivation of *M. aeruginosa* is also studied, including the algal density, humic acid (HA) and pH. When the algal density is  $2.6 \times 10^6 \text{ cells/mL}$ , it reaches the highest algal removal rate compared to  $3.6 \times 10^6$ ,  $4.6 \times 10^6$ ,  $5.6 \times 10^6$ ,  $6.6 \times 10^6$ ,  $7.6 \times 10^6$ ,  $8.6 \times 10^6$ ,  $9.6 \times 10^6$ ,  $1 \times 10^7$ ,  $1 \times 10^8$  and  $1 \times 10^9 \text{ cells/mL}$ , inactivating 91% of *M. aeruginosa* within 150 min (Fig. S13). These results can confirm that the best effect of algal removal is in the early logarithmic growth. Furthermore, the photocatalytic inactivation of algae is not affected in the existence of humic acid and pH (Fig. S14), confirming the excellent stability of Ov-BO/8.0BNO heterojunction composite in the practical wastewater treatment.

Furthermore, the stability and recyclability were also investigated by carrying out the consecutive recycling experiments. After 5 recycling tests, the removal efficiency of chlorophyll can still retain above 84% in 150 min (Fig. 3i). Moreover, the XRD pattern, FTIR spectra and XPS spectra of used photocatalyst show negligible obvious change compare to fresh photocatalyst (Fig. S15). Overall, all the above results indicate that Ov-BO/8.0BNO has excellent stability and exhibits promising prospect in the practical application.

### 3.5. Analysis of the physiological properties of *M. aeruginosa* during the photocatalytic process

#### 3.5.1. Cell morphologies and membrane permeability assessment

To intuitively confirm the damage of algal cells by Ov-BO/8.0BNO during the photocatalysis, the morphology of algal cells is analyzed by employing the SEM images. As displayed in Fig. 4a and S16a, at the beginning of the photocatalytic experiment most of the cell morphology are regular and plump with smooth surfaces, which indicates the algal cells are growing well. After 60 min of photocatalytic reaction, the wrinkles and depressions can be observed on the algal cells and their shapes become irregular (Fig. 4b and S16b). Subsequently, after 150 min of light radiation, the intact algal cells can hardly be observed in Fig. 4c and S16c. this may be due to that the increased ROS will continuously attack the cell membrane, irreversibly damage the cell structure, finally lead to the death of algal cells [28]. The above results further determine the Ov-BO/8.0BNO has the excellent capacity to inactivate algal cells. For further investigating the breakdown of cellular membrane, cell membrane permeability was analyzed by studying the leakage of non-electrolytes ( $\text{OD}_{264}$ ) and electrolytes (mainly  $\text{K}^+$ ) from algal cells in the photocatalytic process. As displayed in Fig. S17, during the photocatalysis by Ov-BO/8.0BNO, the increase of the  $\text{OD}_{264}$  and  $\text{K}^+$  indicate that Ov-BO/8.0BNO can inactivate the algae by affecting the membrane permeability of algal cells, All the above results prove that Ov-BO/8.0BNO can cause serious damage to cell morphology and membrane permeability during the photocatalysis.

#### 3.5.2. Cell organic matters

The content of algal organic substance can reflect the growth state of the algal cells [29]. Hence, three-dimensional fluorescence spectroscopy was carried out to study the variation in the content of extracellular organic matter (EOM) and intracellular organic matter (IOM) during the photocatalysis. Five fluorescence peaks can be observed in the spectra and the peak A, B, C, D and E are corresponding to protein-like, aromatic

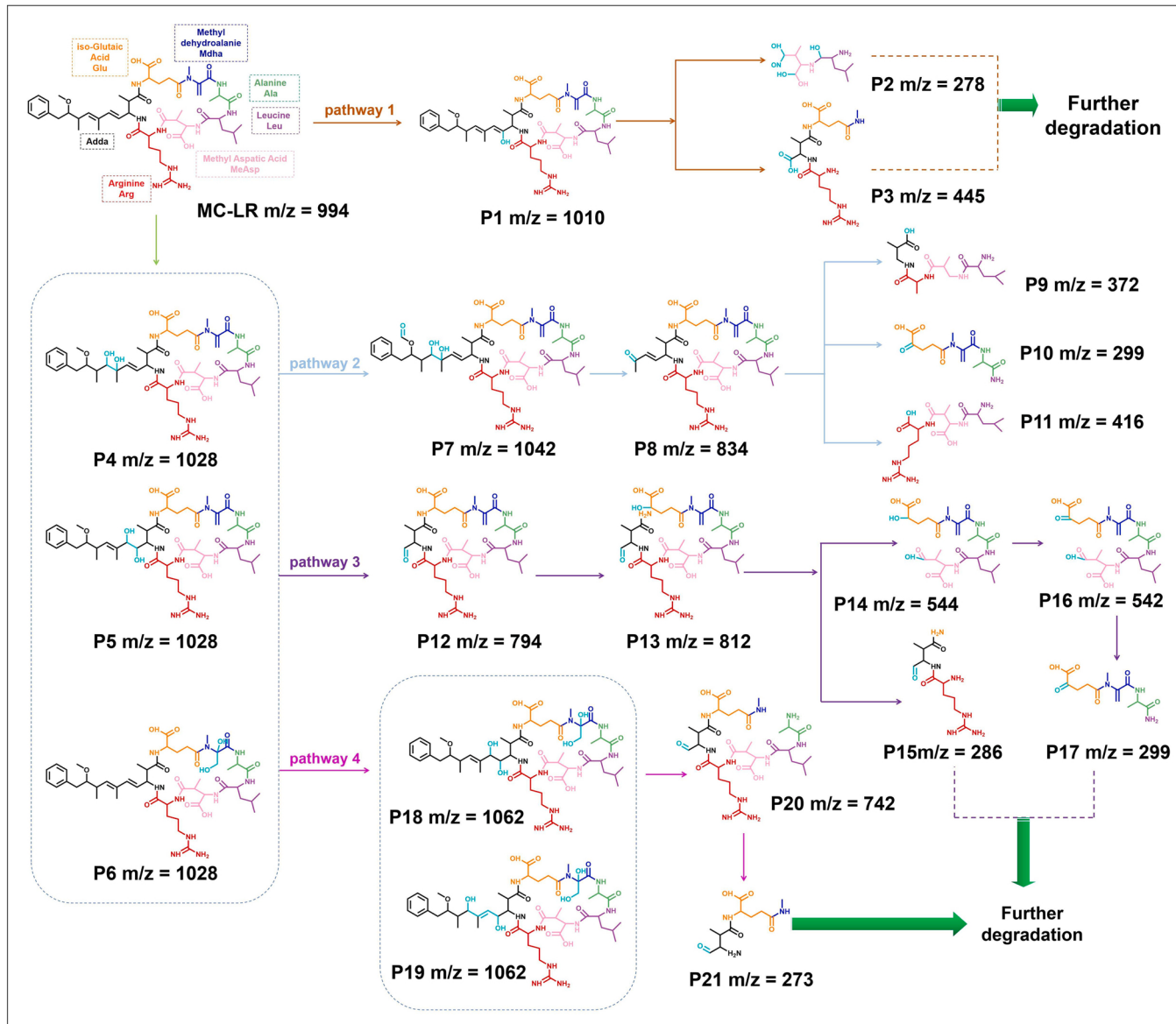


**Fig. 6.** The possible degradation pathway of MC-LR by the Ov-BO/8.0BNO.

protein (tyrosine and tryptophan), soluble microbial by-product, humic acid-like substance and fulvic acid-like substance [30], respectively. In Fig. S18a and S18c, the intensities of peak A, B and C shows no obvious variation, which confirms that under the visible light the Ov-BO and BNO did not restrain the growth of the algae. As for the Ov-BO/8.0BNO, the intensities of peak A, B and C continually increase at the beginning of the experiment, and the intensity of peak obviously decreases after 60 min (Fig. 4d-f and S18b). These results indicate in first 60 min of the photocatalytic process, part of IOM may be let out on account of the damage of algal cells. Then the protein-like matter may turn into soluble microbial by-product. Furthermore, the decreasing trend after 60 min implies the Ov-BO/8.0BNO can degrade organic matter released by algae while inactivating algae, and prevents secondary pollution to a certain extent. Compared with the Ov-BO and BNO, the IOM spectra of the Ov-BO/8.0BNO changes distinctly after 150 min and the intensities of peak A, B, C and D decline visibly (Fig. 4g-i and S19), which indicates the metabolism of algal cells are damaged and algal organelles are destroyed, generating humic and fulvic acid-like matters. Subsequently, all peaks appear apparent drop and the peak C and D can hardly be observed which implies algal cells seriously rupture and abundant IOM

is leaked out. These results can offer the powerful evidence that Ov-BO/8.0BNO can availablely inactivate *M. aeruginosa* and degrade the organics generated by the breakage of cells, which are consistent with the above conclusions.

To more directly investigate the variations of the EOM and IOM in the photocatalytic reaction, the fluorescence regional integration (FRI) partition method was applied to quantitatively study the integral of fluorescence region intensity (Fig. 5a and S20) and the FRI partitioning method and typical representative substances are shown in Table S6. The fluorescence integral values of EOM and IOM by Ov-BO/8.0BNO continues to decrease. These results are consistent with the results of three-dimensional fluorescence spectroscopy. In conclusion, Ov-BO/8.0BNO can validly inactivate algae, and decompose the organics produced by the algae rupture.

### 3.5.3. Phycobiliproteins of algal cells

In photosynthesis system of *M. aeruginosa*, the photosynthetic pigment for harvesting light mainly is the phycobiliproteins (PB), which consist of phycocyanin (PC), allophycocyanin (APC) and phycoerythrin (PE) [1]. Hence, to investigate the influences of the photosynthetic

system by Ov-BO/8.0BNO under visible light, the contents of four proteins of *M. aeruginosa* were carried out. The PC, APC, PE and PB by using the Ov-BO and BNO during the photocatalysis alter slightly (Fig. S21a-b). On the contrary, an obvious decline tendency of the PC, APC, PE and PB can be found during photocatalytic inactivation of algae by Ov-BO/8.0BNO (Fig. 5b). This may be attributed to that the ROS produced by Ov-BO/8.0BNO can impact the phycobiliprotein of *M. aeruginosa* and further destroy the light-harvesting ability of photosynthetic system, leading to the valid inactivation of *M. aeruginosa*. Furthermore, the removal efficiency of chlorophyll b and carotenoids were studied as shown in Fig. S21c-d. During the photocatalysis by Ov-BO/8.0BNO, the chlorophyll b and carotenoids all display an obvious reduce. It indicates that Ov-BO/8.0BNO can disrupt the photosynthetic system of algae cells by destroying the chlorophyll b and carotenoids, which inactivates the algae cells.

### 3.5.4. Antioxidant enzyme system

The two significant antioxidant enzymes in algal cells are SOD and CAT. SOD can convert  $\text{O}_2^-$  to hydrogen peroxide ( $\text{H}_2\text{O}_2$ ) maintaining the body balance and CAT is resistant to oxidative stress from the environment, which can decompose  $\text{H}_2\text{O}_2$  to  $\text{H}_2\text{O}$  and  $\text{O}_2$  thus keeping off the cells from being destructed.

During the photocatalysis by the Ov-BO and BNO, SOD activity is slightly increase in the beginning, and then it gradually decreases (Fig. 5c). The increase of SOD activity may be explained to the stimulation of the visible light and the photocatalysts, and the decrease of SOD activity possibly is related to the adaptation of algae to the environment. Oppositely, the SOD activity during the photocatalysis by the Ov-BO/8.0BNO obviously increases with time process and rapidly reduces after 90 min, indicating the inactivation of algal cells. During the photocatalysis by the Ov-BO and BNO, although a slight increase of the CAT activity appears at first, it then fell back to normal levels (Fig. 5d), which indicate the growth of algal cells is seriously not affected. However, the content of the CAT during the photocatalysis by the Ov-BO/8.0BNO increases gradually in 60 min, arising from the accumulation of  $\text{H}_2\text{O}_2$  produced by the stimulated algal cells. After that, a decrease appears in the CAT activity meaning the ultimately collapsed of antioxidant systems and the death of algal cells. Overall, these results confirm in the presence of Ov-BO/8.0BNO algal cells suffer continuous stimulation and the defense systems are damaged thus eventually leading to the inactivation of algal cells.

### 3.5.5. Lipid peroxidation and metabolic activities of algal cells

The content of MDA is a significant biomarker sign of cellular oxidative injure, directly exhibiting the lipid peroxidation degree of cell membrane. MDA content has slight variation during the photocatalysis by the Ov-BO and BNO, indicating the lesser impact to the algal cells (Fig. 5e). On the contrary, during the photocatalysis by the Ov-BO/8.0BNO, the content of MDA markedly increases within 90 min demonstrating the algal cells are suffered from the serious oxidative stress. Then MDA content obviously declines, arising from the severe lipid peroxidation, the damage of cell membrane and the apoptosis of algal cells.

Furthermore, the total soluble protein can reflect cell metabolic activity. In Fig. 5f, a small decrease appears during the photocatalysis by the Ov-BO and BNO indicating that photocatalyst has a certain effect on protein synthesis under light irradiation. Correspondingly, the total soluble protein content displays an obvious decrease during the photocatalysis by the Ov-BO/8.0BNO, confirming that the algal organelles can be attacked by the ROS generated by the photocatalysts thus lessening the total soluble protein. Hence, the above results can illustrate Ov-BO/8.0BNO can restrain the synthesis of protein, which seriously destroys the physiological metabolism of algae and leads to algae inactivation.

## 3.6. Photocatalytic degradation of MC-LR and the possible degradation pathways

The release of Microcystins-LR (MC-LR) is throughout the growth, metabolism and rupture of the algal cells, which pose the serious harm to the environment and human health. Hence, the photocatalytic degradation experiment of MC-LR by Ov-BO/8.0BNO was carried out. The removal efficiency of Microcystins-LR (MC-LR) by Ov-BO/8.0BNO displays the best photodegradation effect compared with Ov-BO and BNO, which can reach about 96% at 100 min (Fig. S22). These results indicate that the Ov-BO/8.0BNO not only effectively inactive the algal cells, but also remove MC-LR released by algal cells thus avoiding the secondary pollution to some extent. To analyze the photodegradation process of MC-LR in depth, LC-MS techniques were applied to analyze the intermediates of MC-LR (Fig. 6 and Table S7). During the photocatalytic process, various intermediates are detected with  $m/z$  of 1010, 1062, 1042, 1028, 278, 445, 834, 372, 299, 416, 794, 812, 544, 286, 542, 299, 742, 273. Based on the above results, we proposed the four probable degradation pathways of MC-LR by Ov-BO/8.0BNO.

In the pathway 1, the addition reactions will appear at the conjugated double bond, resulting in the isomerization diene bond in the Adda chain and generating intermediate product 1 (P1) [3]. The breakage may firstly emerge at the Adda chain and the conjugated double bond of Mdha amino acids. Then P2 and product P3 are generated because of the breakage of Arg-MeAsp and Ala-Leu peptide bonds [31].

Furthermore, the conjugated double bond of Adda side chain and unsaturated double bond of Mdha moiety may be attacked by ROS, generating dihydroxylated isomers products (P4, P5, P6) [32]. Then, in the pathway 2 the methoxy group in Adda chain is readily oxidized to formic acid-(MC-LR) ester, thus generating the P7 [33]. It will be subsequently oxidized to generate the P8. Afterwards, the P9, P10 and P11 are formed after the broken of Adda-Glu, Ala-Leu and Adda-Arg peptide bonds in the P8.

In the pathway 3, the dihydroxylated isomers P5 can be further oxidized to produce the P12. Then, the P13 may be formed after the broken of hydrolysis of the amino group in the Glu of P12. And the hydrolysis reaction can appear at the Arg, generating the P14 and P15. Then the P16 can be formed by the oxidation of hydroxyl group. Furthermore, the amino group of Leu in intermediate P16 is hydrolyzed to form P17.

In the pathway 4, electrophilic free radical is added to unsaturated double bond in the P6, which forms two tetrahydroxylated isomers (P18 and P19). The Adda and Mdha moieties in the MC-LR peptide chain are further oxidized to form the P20. Then, the P21 is produced by the hydrolysis of P20. In the end, these produced intermediates can be further oxidized and degraded, which confirm the remarkable mineralization capacity of Ov-BO/8.0BNO for MC-LR.

Furthermore, to clarify the preferable degradation pathway of MC-LR, Fukui index based on the density functional theory (DFT) is applied to predict the regioselectivity of reactive oxygen species (ROS) for attacking the MC-LR molecules. The distribution of  $f^+$  and  $f^\circ$  values on MC-LR are shown in Fig. S23 and Table S8. These results show that C12, C15, C34, C37, and O50 are likely to be attacked by reactive species (Fig. S23b). Hence, the pathway 1, pathway 2 and pathway 4 are preferred to occur in these possible routes for the MC-LR degradation.

### 3.7. Toxicity predictions of MC-LR during the degradation process

The aquatic toxicity of MC-LR and transformation intermediates are given in Fig. 7 and Table S8. The acute toxicity is calculated as LC50 for fish and daphnia, and EC50 for green algae, and these data are 15412.44, 1564.94, and 1773.49 mg/L for MC-LR, respectively. In addition, chronic toxicity values (ChVs) of MC-LR are 1463.21, 109.99, and 524.45 mg/L, respectively. Hence, in terms of acute and chronic toxicity according to the aquatic toxicity criteria, MC-LR is not hazarded

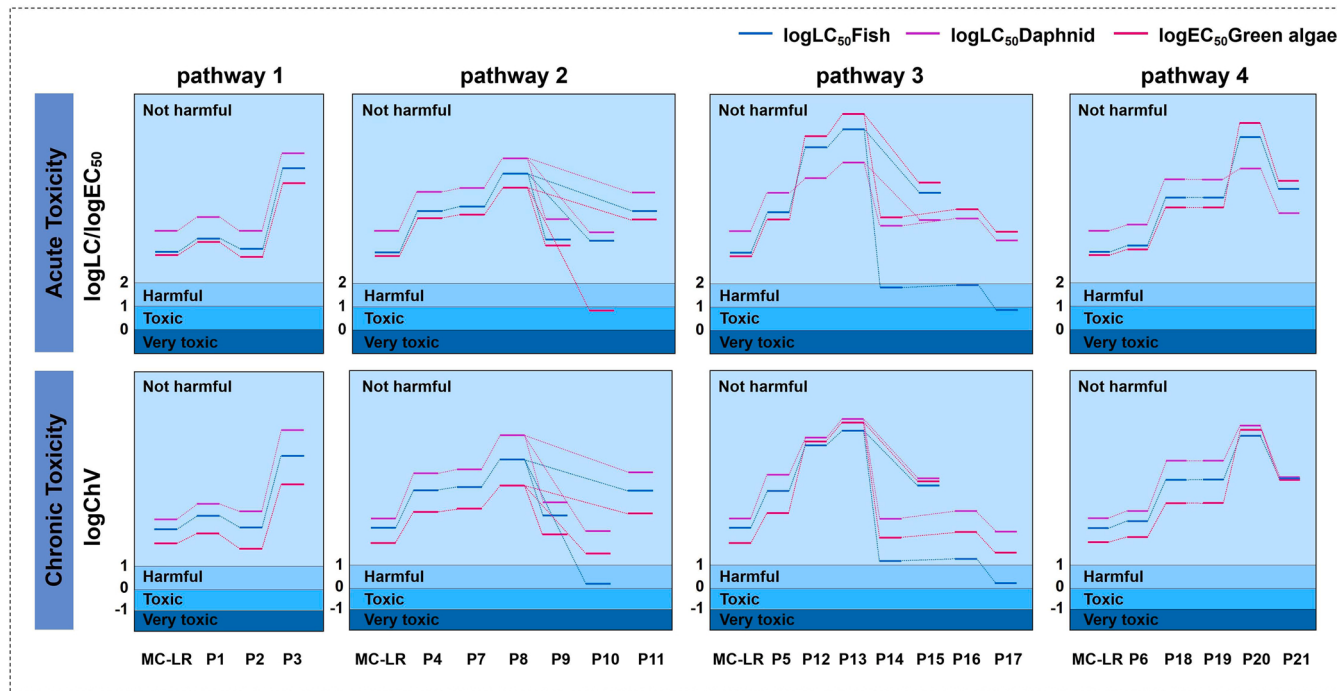


**Fig. 7.** Acute and chronic toxicity evolution of MC-LR and its degradation intermediates toward three aquatic organisms using EPI Suite software with ECO-SAR program.

to aquatic organisms [34].

Considering the chronic and acute toxicities, most intermediates are harmless to fish, daphnia, and green algae apart from P10, P14, P16 and P17. For degradation pathways 1 and 4, at three trophic levels chronic and acute toxicities decreased on the whole. Whereas in pathways 2 and 3 a complex trend of toxicity evolutions of intermediates is observed. Although toxic intermediates will appear during the evolution process, these intermediates can be further detoxified by ROS to produce non-harmful products. These results indicate Ov-BO/8.0BNO catalyst is very effective in detoxifying MC-LR and it will not produce the very toxic products in the photocatalytic degradation of MC-LR.

As a result, based on all the above studies, we propose the schematic diagram of the Ov-BO/8.0BNO for the inactivation of algal cells and photodegradation of MC-LR as displayed in Fig. S24. During the photocatalysis, active substances can irreversibly oxidate the cell walls and membranes, thus resulting in the damage and death of algae. At the same time, the electrolytes, the cellular content, and the metabolites including MC-LR will be divulged and can be further degraded by active substances, which thus validly avoids the potential secondary pollution. In summary, this high-efficiency photocatalyst can achieve the inhibition of algal growth and MC-LR degradation.

Considering of the excellent degradation of organic matter and algal toxins, Ov-BO/8.0BNO should also be good at degrading common organics. Therefore, CIP is selected as a model organic in this study. Ov-BO/8.0BNO displays the highest photodegradation ability of CIP and the removal efficiency reaches 99.9% in 150 min (Fig. S25), which is 16.92 and 18.11 times higher than Ov-BO and BNO, respectively. Furthermore, the optimal dosage of Ov-BO/8.0BNO is determined to be 0.05 g (Fig. S26). The TOC analysis shows the mineralization rate reaches after 67% after 150 min under visible-light illumination, confirming the excellent mineralization ability of Ov-BO/8.0BNO (Fig. S27). Meanwhile, the excellent stability and recyclability are also confirmed by carrying out the consecutive recycling experiments, the XRD pattern and XPS spectra of used photocatalyst (Fig. S28). Furthermore, the possible degradation pathways of CIP is proposed by the LC-MS techniques (Fig. S29).

#### 4. Conclusion

To sum up, using Ov-BO/BNO VDW heterojunction with plenty of OVAs as a model system, we have confirmed the construction of VDW heterojunction can enhance photocatalytic  $O_2$  activation, displaying excellent photocatalytic ability on algal cells inactivation and degradation of MC-LR. The IS-XPS and DFT calculation indicate the strong electronic coupling interactions are presented between BNO and Ov-BO by VDW forces. Moreover, XPS and EPR analysis confirm that a mass of OVAs presented in Ov-BO/BNO VDW heterojunction, and OVAs can be used as the electron trapping centers to speed up chemisorption of  $O_2$ . Furthermore, the VDW force will drive the photoelectrons in CB of  $Bi_3NbO_7$  transfer to VB of  $BiO_{2-x}$  through S-scheme transfer path. Electrochemical and photochemical results further uncover the separation and transfer processes of charge are efficiently enhanced, thus increasing the number of electrons transferred from photocatalyst to  $O_2$  and leading to generate more  $O_2$ . Besides, the photocatalytic inactivation of algae by Ov-BO/8.0BNO is 14.17 and 19.05 times higher than Ov-BO and BNO, respectively. By the analysis of LC-MS techniques, four possible photodegradation pathways of MC-LR are proposed and the Adda chain and Mdha amino in MC-LR are vulnerable to suffer from attacking by the ROS. Furthermore, the results of the aquatic toxicity indicate Ov-BO/8.0BNO catalyst is very effective in detoxifying MC-LR and it will not produce the very toxic products in the photodegradation of MC-LR. During the  $O_2$ -dominated photocatalysis, the ROS will destroy the antioxidant system of algal cells and damage the cell membrane, causing the release of organic matters and ions, the collapse of photosynthetic system and the final death of algal cells. This work offers new thinking in the enhancement of photocatalytic  $O_2$  activation and provides a design avenue to synthesize novel 2D/2D VDW heterojunctions photocatalysis for the treatment of cyanobacterial blooms in the eutrophic water bodies.

#### CRediT authorship contribution statement

**Dongyu Xu:** Investigation, Writing – original draft, Formal analysis.  
**Geng Li:** Methodology; **Yilin Dong:** Writing – review & editing.

**Qiuwen Wang:** Validation. **Jie Zhang:** Investigation; **Tongsa Yang:** Conceptualization. **Shaoxuan Pang:** Investigation. **Guangming Zhang:** Supervision; **Longyi Lv:** Investigation. **Yuguo Xia:** Software. **Zhijun Ren:** Supervision, Funding acquisition; **Pengfei Wang:** Supervision, Funding acquisition, Writing – review & editing.

### Declaration of Competing Interest

The authors declare that they have no known competing financial interests or personal relationships that could have appeared to influence the work reported in this paper.

### Acknowledgements

The authors gratefully acknowledge the financially support by the National Natural Science Foundation of China as general projects (grant No. 51779068 and 22006029), the Natural Science Foundation of Hebei Province (grant No. B2019202078), Science and Technology Research Projects of Colleges and Universities in Hebei Province (grant No. ZD2020149), and this research was supported by Open Research Fund of CNMGE Platform & NSCC-TJ (grant No. CNMGE202101010).

### Appendix A. Supporting information

Supplementary data associated with this article can be found in the online version at [doi:10.1016/j.apcatb.2022.121402](https://doi.org/10.1016/j.apcatb.2022.121402).

### References

- [1] G. Fan, Y. You, B. Wang, S. Wu, Z. Zhang, X. Zheng, M. Bao, J. Zhan, *Appl. Catal. B: Environ.* 256 (2019), 117866.
- [2] G. Fan, Z. Chen, S. Gu, B. Du, L. Wang, *Chemosphere* 284 (2021), 131283.
- [3] M. Nawa, M. Moztahida, J. Kim, A. Shahzad, J. Jang, W. Miran, D.S. Lee, *Carbohydr. Polym.* 199 (2018) 109–118.
- [4] H. Huang, S. Tu, C. Zeng, T. Zhang, A.H. Reshak, Y. Zhang, *Angew. Chem. Int. Ed.* 56 (2017) 11860–11864.
- [5] Y. Mao, P. Wang, L. Li, Z. Chen, H. Wang, Y. Li, S. Zhan, *Angew. Chem. Int. Ed.* 59 (2020) 3685–3690.
- [6] S. Chen, H. Wang, Z. Kang, S. Jin, X. Zhang, X. Zheng, Z. Qi, J. Zhu, B. Pan, Y. Xie, *Nat. Commun.* 10 (2019) 788–795.
- [7] J. Li, Z. Xia, M. Zhang, S. Zhang, J. Li, Y. Ma, Y. Qu, J. Mater. Chem. A 7 (2019) 17974–17980.
- [8] L. Liang, F. Lei, S. Gao, Y. Sun, X. Jiao, J. Wu, S. Qamar, Y. Xie, *Angew. Chem. Int. Ed.* 54 (2015) 13971–13974.
- [9] Yating Wang, J. Cai, M. Wu, J. Chen, W. Zhao, Y. Tian, T. Ding, J. Zhang, Z. Jiang, X. Li, *Appl. Catal. B: Environ.* 239 (2018) 398–407.
- [10] D. Liu, D. Chen, N. Li, Q. Xu, H. Li, J. He, J. Lu, *Angew. Chem. Int. Ed.* 59 (2020) 4519–4524.
- [11] R. Li, Q. Luan, C. Dong, W. Dong, W. Tang, G. Wang, Y. Lu, *Appl. Catal. B: Environ.* 286 (2021), 119832.
- [12] P. Wang, Y. Mao, L. Li, Z. Shen, X. Luo, K. Wu, P. an, H. Wang, L. Su, Y. Li, S. Zhan, *Angew. Chem. Int. Ed.* 58 (2019) 11329–11334.
- [13] M. Li, P. Wang, Z. Ji, Z. Zhou, Y. Xia, Y. Li, S. Zhan, *Appl. Catal. B: Environ.* 289 (2021), 120020.
- [14] K. Crowley, G. Ye, R. He, K. Abbas, X.P.A. Gao, *ACS Appl. Nano Mater.* 1 (2018) 6407–6413.
- [15] M.-Y. Yan, Z.-Y. Jiang, J.-M. Zheng, Y.-M. Lin, Z.-Y. Zhang, *Appl. Surf. Sci.* 531 (2020), 147318.
- [16] P.E. Blochl, *Phys. Rev. B* 50 (1994) 17953–17979.
- [17] G. Kresse, J. Furthmüller, *Comput. Mater. Sci.* 6 (1996) 15–50.
- [18] J.P. Perdew, K. Burke, M. Ernzerhof, *Phys. Rev. Lett.* 77 (1996) 3865–3868.
- [19] J. Ran, W. Guo, H. Wang, B. Zhu, J. Yu, S.-Z. Qiao, *Adv. Mater.* (2018) 1800128.
- [20] J. Wang, Z. Liu, Z. Liu, *Solid State Sci.* 95 (2019), 105935.
- [21] D. Xu, H. Feng, Y. Dong, Q. Wang, G. Zhang, L. Lv, Z. Ren, P. Wang, *Adv. Mater. Interfaces* (2020) 2000548.
- [22] L. Zhou, X. Zhang, M. Cai, N. Cui, G. Chen, G. Zou, *Appl. Catal. B: Environ.* 302 (2022), 120868.
- [23] K. Wang, Y. Li, G. Zhang, J. Li, X. Wu, *Appl. Catal. B: Environ.* 240 (2019) 39–49.
- [24] R. Jiang, D. Wu, G. Lu, Z. Yan, J. Liu, *Chemosphere* 227 (2019) 82–92.
- [25] J. Wang, Y. Yu, J. Cui, X. Li, Y. Zhang, C. Wang, X. Yu, J. Ye, *Appl. Catal. B: Environ.* 301 (2022), 120814.
- [26] P. Wang, Z. Shen, Y. Xia, H. Wang, L. Zheng, W. Xi, S. Zhan, *Adv. Funct. Mater.* 29 (2019) 1807013.
- [27] B.D. Amadu, D. Xu, Q. Zhang, Z. Zhang, Q. Wang, Y. Dong, G. Zhang, Z. Ren, P. Wang, *J. Taiwan Inst. Chem. E.* 125 (2021) 78–87.
- [28] G. Fan, Z. Chen, Z. Yan, B. Du, H. Pang, D. Tang, J. Luo, J. Lin, J. Hazard. Mater. 409 (2021), 125018.
- [29] Z. Yan, F. Qu, H. Liang, H. Yu, H. Pang, H. Rong, G. Fan, B.Vd Bruggen, *J. Membr. Sci.* 617 (2021), 118638.
- [30] G. Fan, X. Li, X. Chen, Y. You, W. Dai, F. Qu, D. Tang, Z. Yan, *Chem. Eng. J.* 427 (2022), 132005.
- [31] X. Hua, X. Hua, C. Tanga, S. Wen, X. Wu, J. Long, X. Yang, H. Wang, L. Zhou, *Chem. Eng. J.* 330 (2017) 355–371.
- [32] G. Fan, Y. You, Z. Yan, M. Xia, L. Hong, B. Du, J. Luo, H. Pang, *J. Water Process. Eng.* 39 (2021).
- [33] Y. Su, Y. Deng, Y. Du, J. Mol. Catal. A: Chem. 373 (2013) 18–24.
- [34] Y. Gao, T. An, H. Fang, Y. Ji, G. Li, *J. Hazard. Mater.* 278 (2014) 417–425.